Development of Safeguards Instrumentation and Techniques at the Idaho National Laboratory for an Electrochemical Facility

Ammon N. Williams, Guoping Cao, Brian Westphal, Greg Galbreth, Jeff Sanders, David Sell, Shelly Li, Natalie Gese, Brenda Serrano-Rodriguez

Idaho National Laboratory
1955 N. Fremont Ave.
Idaho Falls, ID 83415

Abstract

The United States (U.S.) Department of Energy (DOE) Materials Protection, Accounting, and Controls Technology (MPACT) campaign has been developing a Virtual Facility Distributed Test Bed of an electrochemical reprocessing facility, specifically with Safeguards and Security by Design (SSBD) in mind. At Idaho National Laboratory (INL), four measurement technologies are under development to support the MPACT Virtual Facility Distributed Test Bed. These technologies are oxide reduction (OR) voltammetry, an electrorefiner (ER) actinide sensor, a triple bubbler, and uranium and transuranic (U/TRU) measurements using a thermocouple. Laboratory and/or field-testing for each of these technologies is presented, including measurement uncertainties where applicable.

1 Introduction

Under the United States (U.S.) Department of Energy (DOE) Materials Protection, Accounting, and Control Technologies (MPACT) campaign, a Virtual Facility Distributed Test Bed is under development to explore Safeguards and Security by Design (SSBD) of a virtual electrochemical facility. Technologies utilized in this virtual facility are under development across the U.S. national laboratory complexes and universities. A description of the Virtual Facility Distributed Test Bed and a summary of all the different technologies under development within the MPACT campaign can be found elsewhere.[1]

In the electrochemical (i.e., pyroprocessing) approach chosen for investigation in the virtual facility, the used oxide fuel is first declad and then reduced to metallic form in the oxide reduction (OR) process in a lithium chloride (LiCl)-1 wt% lithium oxide (Li_2O) salt electrolyte. To confirm that the OR system in the process is operating as declared and within normal parameters, an OR voltammetry probe has been proposed to provide process monitoring data and is under development at Idaho National Laboratory (INL). Following the OR process, the basket containing the metallic fuel is loaded into the electrorefiner (ER) were the uranium (U) metal is electrochemically dissolved from the anode and deposited on the cathode. Actinide chlorides are expected to be present in the ER electrolyte, and means to monitor the salt composition qualitatively and quantitatively are necessary. Three technologies to monitor the actinide content of the ER are being developed under MPACT. They are the ER voltammetry probe and microfluidic sampling at Argonne National Laboratory (ANL)[2] and the actinide sensor at INL. In addition to the measurement technologies being investigated to measure the composition of the

ER electrolyte, the triple bubbler sensor is being developed at INL to measure the density and depth of the salt with the purpose of determining the overall salt volume necessary to determine the total mass of special nuclear materials contained in the ER vessel. As part of the electrorefining process, plutonium (Pu) builds up in the electrolyte and is periodically removed in tandem with U in a process called U/transuranic (TRU) extraction. A measurement method developed at INL uses a thermocouple approach to determine the Pu fraction in the U/TRU product during solidification.

In this work, the four measurement technologies being developed at INL will be discussed in detail. These technologies are OR voltammetry, ER actinide sensor, triple bubbler, and U/TRU measurements using a thermocouple. In the following sections, each technology with current results and uncertainties will be discussed.

2 Oxide Reduction Voltammetry

In the OR process, used nuclear oxide fuel is loaded into a cathode basket, immersed into a LiCl-Li_2O salt electrolyte, and electrolytically reduced to metal form while oxygen (O_2) forms on the anode. During this process, fission products from the fuel dissolve into the electrolyte while the rare-earth and actinides in the fuel are converted to metallic form and stay within the cathode basket. Thus, under normal operating conditions, actinide chlorides are not expected to be present in the OR salt. However, to ensure timely detection or misuse of the facility and process, a voltammetry probe has been proposed to monitor the OR electrolyte. Voltammetry methods, particularly cyclic voltammetry (CV), have been widely used to measure thermodynamic properties and constituents in molten salt.[3-6] At INL, a voltammetry probe for use in LiCl-Li_2O salt has been in development under the MPACT program. Efforts have focused on the development of electrode materials that were capable of long-term operation in the OR electrolyte that provided suitable detection ability. Williams et al.[7] explored tungsten (W), tantalum (Ta), platinum (Pt), stainless steel (SS), molybdenum (Mo), and iridium (Ir) as working electrodes (WEs) and found that SS, Pt, and Ir were the most promising materials for long-term WE materials. The goal of the current study was to evaluate WE performance in an actual OR system at INL and to assess the voltammetry technique in realistic conditions. The approach was to construct a voltammetry probe with integrated electrodes, install it in an actual OR system at INL, and then monitor the OR system over time while evaluating probe performance.

2.1 Experimental Setup

An OR voltammetry probe was constructed as shown in Figure 1. The structure of the probe was a magnesium oxide (MgO) tube with four holes down its axis. Two of the holes were sealed on the bottom with porous MgO plugs and contained redundant nickel-nickel oxide (Ni/NiO) reference electrodes (REs). Through the other two holes, 1.6 mm diameter SS and Ir wires were used as WEs (i.e., approximately 25 mm of wire was exposed). The entire MgO assembly containing the REs and WEs was slid into a 316 SS tube. The SS tube provided structural support in addition to functioning as the counter electrode (CE). When installed in the OR, the SS CE was submerged approximately 15 cm into the salt.

Figure 1. Photo of the OR voltammetry probe used in field-testing.

Testing used a three-electrode configuration; thus, only one of the WEs in the probe was active at a time. In each measurement session, a series of CV measurements were acquired using the SS WE followed by the Ir WE. Between each CV, open circuit potential (OCP) was acquired for three to five minutes. The vertex potentials for the SS WE were -0.2 V and -1.65 V, just past the Li reduction potential. For Ir, the vertex potentials were 1.1 V, past the Ir oxidation potential, and -1.65 V, just past the lithium (Li) reduction potential.

The OR system used in these field-tests principally contained LiCl salt with 1 wt% Li_2O operated at 650°C. As the OR had been used to process used nuclear fuel, fission product chlorides were also present in the salt. Once the voltammetry probe was installed in the salt, leads were connected to each electrode at the top of the probe using banana jacks. These leads passed through the hotcell wall and to a junction box where potentiostat leads could be connected. The total lead length was unknown, but was estimated to be 10–15 meters in length. To reduce the effect of voltage drop through the lines, a sense line was used in parallel to the working lead and connected at the top of the OR voltammetry sensor. The potentiostat used in field-testing was a Moldulab XM with a 2 A booster (Solartron Analytical). The potentiostat was set in a floating configuration.

2.2 Results and Discussion

Representative CV scans taken over several weeks in the OR are shown in Figure 2. There is a notable slope (I vs. V) to all CV scans. A slope in a CV scan is typically an indicator of resistance between the electrodes with the slope of the V vs. I lines being a measure of the resistance. From the slope of the CV scans, it appears the resistance was approximately two to three ohms for the Ir leads and one to two ohms for the SS. The voltammetry leads from the potentiostat to the probe were checked using a 1 kΩ dummy cell and no issues were discovered. The reason for the extra resistance is unknown. However, in lab testing, hairline cracks were observed in the MgO due to thermal shocking. If similar hairline cracks occurred below the salt line of the probe, it may be possible that a minor short developed between the electrodes, which contributed to the sloped CV scans.

The CV measurements taken on the SS WE are shown in Figures 2a and 2b. Two potential windows were explored—in the first, the vertex potential was past the Li reduction potential (see Figure 2a), and in the second, the vertex potential was just short of the Li reduction potential (see Figure 2b). The CV runs on SS after sitting in the salt for several hours had large reduction like

currents that decreased with every cycle and usually cleared up within the first four to five cycles. Over the five-week measurements shown, the Li reduction potential did shift approximately 50 mV total. Additionally, outside of the first week, all the CV measurements were quite repeatable. Li oxidation peak varies in height proportionately to the amount of Li reduced. In general, these CVs appear to be relatively free of features.

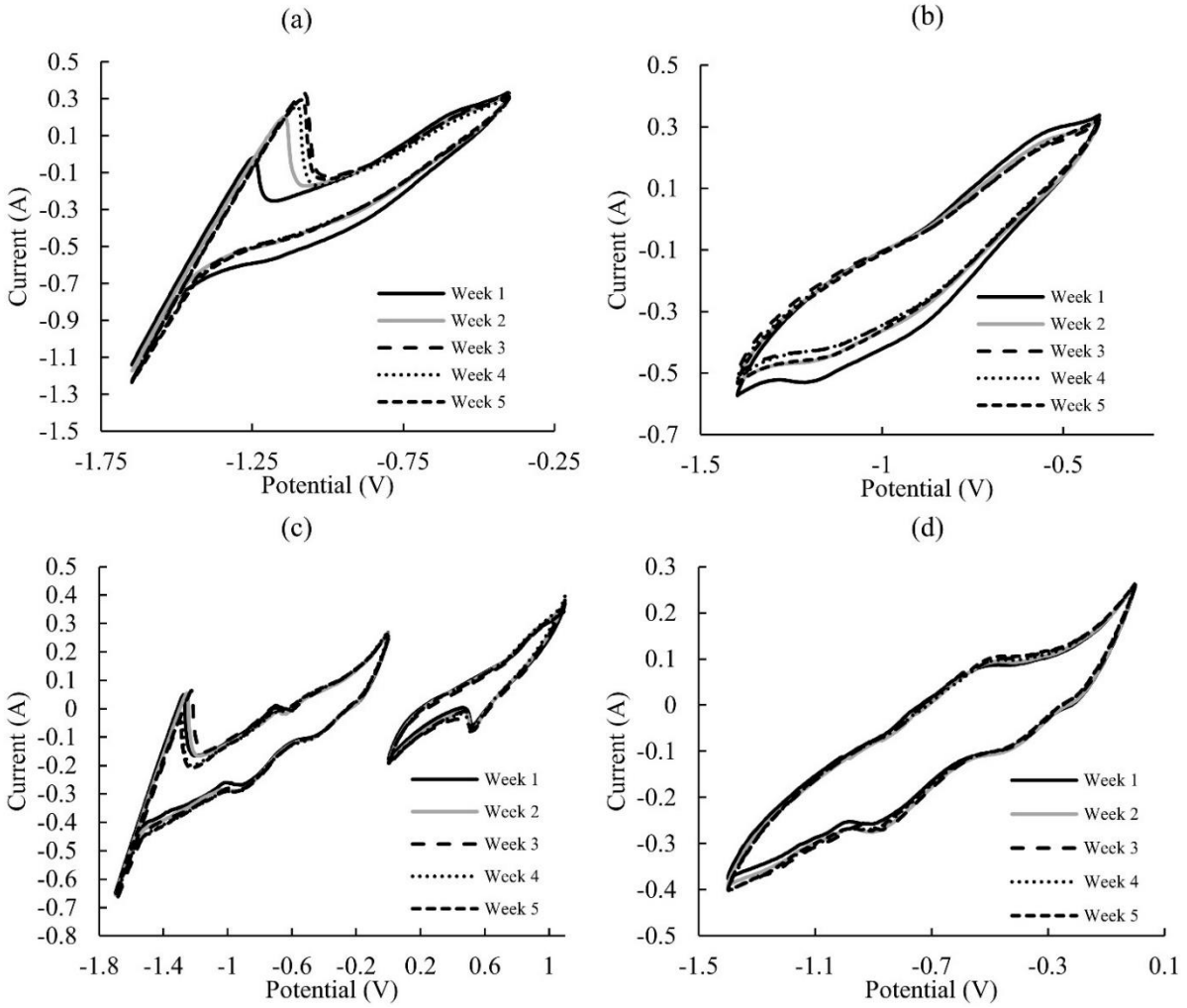

Figure 2. CV measurements taken in an OR system at INL, the CE was SS, the RE was Ni/NiO, and the scan rate was 25 mV/s. (a) SS WE full potential window; (b) SS WE region of interest; (c) Ir WE full potential window; and (d) Ir WE region of interest.

Figures 2c and 2d shows the CV results from the Ir WE. In Figure 2c, both the cathodic and anodic scans are shown. From the cathodic scan, the Li reduction potential shifted in a similar manner as observed on the SS WE. In addition, a reduction peak starting at approximately −0.65 V appeared and is thought to be the result of lithium hydroxide (LiOH) or other contaminants due to moisture absorption into the salt.[8-9] This same feature was also observed in many of the laboratory experiments.[7] In the anodic potentials, there is a peak observed around 0.7 V and is thought to be the O_2 oxidation peak. In these scans, there does not appear to be a clear Ir oxidation peak. CV scans are shown in Figure 2d that were collected in the cathodic

potential range with a vertex just short of the Li reduction potential. These scans indicate many of the same features as explained above. The scans also demonstrate the good repeatability of these measurements over time in the OR system.

The OR voltammetry probe has been continuously immersed in the OR at INL for nine months. Though data collection in these tests were not continuous over this period, CV scans were taken on each electrode at least weekly. Outside of the redox features noted above, there were no additional features observed in the data that would indicate the presence of rare earth or actinide chlorides in the OR salt. This observation was consistent with analytical data collected during that period. In addition, for the duration of the field-testing, no noticeable degradation of the electrodes or CV scans were observed.

Overall, the field-testing has demonstrated suitable material selection for long-term monitoring of the OR salt. Future laboratory experiments are planned in which a simulated OR salt will be spiked with different chloride salts including rare earth chlorides and uranium chloride (UCl_3) to explore the sensitivity of the probe and method of detecting varying amounts of these components in an OR salt system.

2.3 Summary

An OR voltammetry sensor/probe has been constructed and field-tested in an oxide reduction system at INL. During the nine months of continuous immersion in the salt and through the weekly CV scans, there has been no noticeable degradation of the sensor signal, nor has there been any indication of salt components beyond those expected (e.g., LiCl, Li_2O, and potentially LiOH). The purpose of the probe is to provide qualitative process monitoring data for the verification of facility operations, which the current sensor does well. Additional studies are currently being conducted to determine the probe sensitivity to rare earth and actinide chlorides to provide an estimate on rare earth and actinide chloride detection limits in the OR salt.

3 Electrorefiner Actinide Sensor

Electrorefining is a critical step in pyroprocessing in which U and other active elements (i.e., lanthanides and transuranics) are oxidized at the anode while U is reduced at the cathode**Error! Reference source not found.**. As a result, the U concentration shifts throughout the operation while the Pu concentration increases. For nuclear material accountancy purposes, it is necessary to know the concentrations of UCl_3 and plutonium chloride ($PuCl_3$) in the potassium chloride (KCl)-LiCl-UCl_3 ER salt. An in situ electrochemical actinide sensor was proposed by INL that has the potential to selectively monitor the UCl_3 and $PuCl_3$ concentrations in the ER. Figure 3 shows a schematic of the proposed electrochemical actinide sensor for monitoring of UCl_3 in a LiCl-KCl-UCl_3 salt system. The sensor consists of an silver/silver chloride (Ag/AgCl) RE with fixed electrode potential and a U-β" alumina membrane electrode that is only sensitive to uranium ion (U^{3+}) concentration changes. A potential is formed across the U-membrane wall due to the U^{3+} activity difference between the inside reference salt (e.g., LiCl-KCl salt containing a fixed concentration of UCl_3) and the test salt outside the U-β" alumina membrane. This potential changes with the UCl_3 concentration—or activity to be more precise—in the test salt. Thus, any change in the UCl_3 concentration in the salt has the effect of shifting the OCP between the RE

and U-β” alumina membrane electrode. The OCP of the electrochemical cell in Figure 3 can be expressed as:

$$\Delta E = \frac{RT}{3F}\left(lna_{U^{3+}(ref)} - lna_{U^{3+}(ws)}\right) + Constant = A - Blna_{U^{3+}(ws)} \quad (1)$$

where ΔE is the cell potential (V), R is the molar gas constant (8.314 J $mol^{-1}K^{-1}$), T is absolute temperature (K), a is activity, *ref* is the reference salt solution (constant), *ws* is the work solution (or test salt the composition of which is unknown), and both A and B are constants.

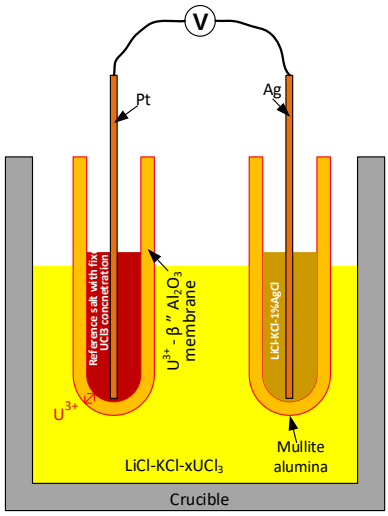

Figure 3. Schematic of an electrochemical cell to measure OCP with a U-β” alumina membrane and Ag/AgCl RE in LiCl-KCl-UCl_3 salt.

A key component in the design was a U-β” alumina membrane, which was made by ion exchange. Ion exchange is an old technology in which cations within the material structure are exchanged for a different cation. A potential material to develop a U-membrane is sodium (Na)-β” alumina. This material is easily ion exchanged in different salts including nitrates and chlorides[10-12]. Ion exchange of Na-β” alumina was also reported in recent years, mainly for battery applications.[13-16] If the sodium ions (Na^+) in the Na-β” alumina can be successfully exchanged with U^{3+} ions, a suitable U-membrane may result that is only conductive to U^{3+} ions. The approach in this current study was to develop a U-β” alumina membrane material, fabricate an electrochemical actinide sensor, and test it in a LiCl-KCl-UCl_3 salt system to evaluate the sensor OCP response to changes in the UCl_3 and other chloride salt concentrations in a surrogate ER salt system.

3.1 Method

The ion selective U-β” alumina membrane tube was made by ion exchange of Na-β” alumina in UCl_3 salt at elevated temperature, usually below the melting point of UCl_3 at 837°C. Several different temperatures (e.g., 650°C, 680°C, and 735°C) were selected for ion exchange in UCl_3, while the duration for the ion exchange was typically 150–300 hours. The Na- β” alumina precursors, fabricated by an electrophoretic deposition (EPD) process, were procured from

Ionotec of the United Kingdom (UK). The dimensions were 4 or 6.5 mm of inner diameter (ID) and 0.5 or 1.0 mm of wall thickness. Details about the Ionotec Na- β" alumina precursors can be found on the company's website.[17]

To prepare the ion exchange process, a Na-β" alumina precursor tube was loaded into a quartz tube with a closed end. Then, UCl_3 salt powder was added into the quartz tube, with the Na-β" alumina tube fully covered by the UCl_3 salt. The top of the quartz tube was covered by a custom fabricated Macor ceramic lid. The quartz tube with the Na-β" alumina tube and UCl_3 salt was then slowly (e.g., less than 5°C/min) heated to and held at the predetermined ion exchange temperature. After the ion exchange process, the furnace for ion exchange was slowly cooled down to room temperature. Water was used to clean away the salt inside and outside the β" alumina tube. After washing, the U-β" alumina tube was then subjected to an annealing process of 800°C for about 10 hours.

After the U-β" alumina tubes were fabricated and inspected, a U-sensor electrode was assembled as shown in Figure 4, which shows the components for assembling a U-sensor electrode and a U–sensor electrode ready for testing. The U-β" alumina membrane tube was filled with a small amount of LiCl-KCl-79.3wt%UCl_3 reference salt, and the electrode in the reference salt was a 0.5 mm diameter Pt wire, which was spot welded to the inside of SS tubing, due to the high cost of Pt wire.

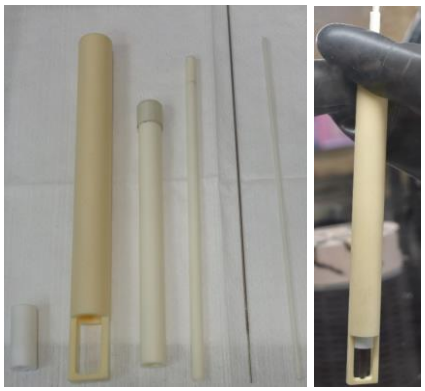

Figure 4. Picture of components for assembling a U-sensor electrode and a U-sensor electrode ready for testing.

During sensor testing, the U-sensor electrode and Ag/AgCl RE (e.g., an silver (Ag) wire in LiCl-KCl-1 wt% AgCl salt contained in a mullite tube) were immersed in LiCl-KCl-0.2 wt% UCl_3 salt for sufficient time so that a stable equilibrium OCP reading was achieved. Then, small amounts of LiCl-KCl-79.3 wt% UCl_3 salt were incrementally added into the salt while the OCP was continuously recorded. Small amounts of lanthanum chloride ($LaCl_3$) and cerium chloride ($CeCl_3$) salts were added to evaluate the selectivity of the UCl_3 sensor.

3.2 Results and Discussion

3.2.1 Fabrication of U-B" Alumina

Initial attempts to fabricate a U-membrane by ion exchange at relatively low temperatures were not successful. The first U-β" alumina tubes made by ion exchange at 650°C for 300 hours shattered completely during the water cleaning process. The likely reason for the shattering of

the U-β” alumina tube was stress accumulation during the ion exchange process. In the ion exchange process, three Na^+ ions were replaced by one U^{3+} ion, causing stress in the material that was unable to relax at 650°C. When the ion exchange temperature was increased from 650–680°C, the U-β” alumina tube (i.e., a 6.5 mm ID and 0.5 mm wall) did not shatter completely during the water cleaning process. However, visual inspection revealed hairline cracking and minor spalling on the material surface. This suggested that at 680°C, there is still significant stress in the U-β” alumina tubes. It may be possible to relieve some of this stress by a high temperature annealing process, such as 800°C for 10 hours.

Finally, successful U-β” alumina tubes were made at 735°C. Following the washing step, no cracks or spalling were observed. In addition, there appeared to be only minor chemical reactions that occurred on the surface of the material. Figure 5 shows two U-β” alumina tubes that were successfully ion exchanged in UCl_3 at 735°C. The average weight gain after ion exchange followed by water cleaning and annealing was about 15%. Theoretically, a complete ion exchange process should increase the material weight by 15.14%. As a result, it appears that almost all the Na^+ ions in the Na-β” alumina were replaced by the U^{3+} from the UCl_3 salt. Complete ion exchange is important as the Na-β” alumina itself exhibits poor compatibility with LiCl-KCl-UCl_3 salt.

Figure 5. Pictures of two U-β” alumina tubes (e.g., both with 1 mm wall thickness) made by ion exchange in UCl_3 salt at 735°C for 120 hours.

After analyzing the results of the U-β” alumina made from ion exchange of Na- β” alumina precursors in solid UCl_3 salt, two other ion exchange options were also explored, where the goal was to minimize the stress accumulation during the ion exchange process and produce a higher strength U-β” alumina membrane. One option was ion exchange in solid UCl_3 of a high strength Na-β” alumina material that was made by Materials & Systems Research Inc. (MSRI). It has been reported that the high strength Na-β” material does not react with moisture and carbon dioxide, which results in superior mechanical properties over the Ionotec material used above. More details about the high strength Na-alumina materials including fabrication and application can be found in the literature.[16] It was expected that this material would be significantly more crack-resistant due to the 30-40 vol% yttria-stabilized zirconia (YSZ) it contains, which provides a more crack-resistant structure. In addition, in this material, the concentration of sodium oxide (Na_2O) is significantly lower than in the Ionotec Na-β” alumina. Thus, the mass of Na^+ that could be ion-exchanged with the U^{3+} ion was much lower, leading to lower stress accumulation. An ion exchange experiment using a sample disc of high strength Na-β” alumina and the ionotec Na-β” was carried out to compare the cracking resistance between the two materials. The samples were immersed in LiCl-KCl-79.3wt% UCl_3 salt at 500°C for 100 hours. Figure 6 shows

a comparison between the high strength Na-β" alumina and the Ionotec Na-β" alumina after testing at 500°C, both in LiCl-KCl-79.3wt%UCl_3 salt. After the high strength Na-β" alumina disc was immersed in LiCl-KCl-79.3wt% UCl_3 ternary salt for 100 hours, no cracks were observed in the material, but the Ionotec Na-β" alumina disc shattered into several pieces after only 50 hours. This shows that the high strength alumina disc was much more crack-resistant than the Ionotec Na-β" alumina.

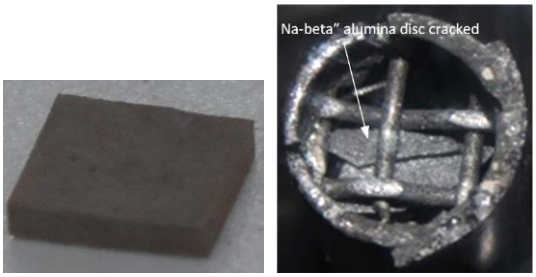

(a) (b)

Figure 6. Photos of two different Na-β" alumina materials that were immersed in LiCl-KCl-79.3 wt% UCl_3 salts: (a) high strength Na-β" alumina disc, about 6 mm x 5 mm x 1 mm, cut from a disc donated from MSRI, no cracks were observed after ion exchange; and (b) Ionotec Na-β" alumina disc, about 20 mm diameter and 0.5 mm thickness from Ionotec shattered during ion exchange.

The other ion exchange option of Na-β" alumina is in UCl_3 vapor. Two advantages to this approach are that the water cleaning step after ion exchange in UCl_3 vapor is not necessary, while the stress formed due to the ion exchange between the Na^+ ion and the U^{3+} ion can be sufficiently released without a specific annealing step. An Ionotec Na-β" alumina tube was ion-exchanged in UCl_3 vapor at 920°C. Figure 7 shows a photograph of the U-β" alumina tube that was ion-exchanged in the vapor phase above UCl_3 salt. No chemical reactions between the UCl_3 vapor and β" alumina were observed. It also appears that the mechanical strength of the U-β" alumina after ion exchange had not decreased. The likely reason for the mechanical strength being retained was that at the high temperature of 920°C, the stress due to the ion exchange process was sufficiently relaxed. Additionally, in contrast to the U-β" alumina made by ion exchange in solid UCl_3 salt, no water cleaning was needed after ion exchange because the inside and outside of the tube was essentially salt free, and therefore, the fabricated U-β" alumina tube can be directly used for U-sensor testing.

Figure 7. A picture of a Na-β" alumina tube (e.g., 6.5 mm ID, 0.5 mm wall, and 30 mm long) that was ion-exchanged in salt vapor above UCl_3 salt. No water cleaning and annealing were used after the ion exchange.

As shown above, the ion exchange in the UCl_3 vapor phase and ion exchange of high strength Na-β" alumina appear very promising for producing high quality ion selective U-β" alumina

membranes that are of high strength and chemical reaction free. Unfortunately, due to project limitations, only preliminary work was performed in the ion exchange of high strength Na-β" alumina materials and ion exchange of Na-β" alumina in a high temperature UCl_3 vapor phase. For the remainder of the work, the ion U-β" alumina membranes used to manufacture the ER actinide sensors used in this study were made from ion exchange of Ionotec Na-β" alumina using solid UCl_3 at 735°C.

3.2.2 Sensor Test Results

Figure 8 shows the OCP measured between a U-sensor electrode and an Ag/AgCl RE when UCl_3 salt concentrations were changed. This shows that the U-β" alumina membrane (e.g., 4 mm ID × 1 mm wall thickness × 30 mm long) can respond to the UCl_3 concentration changes. The initial LiCl-KCl-UCl_3 salt had 0.43 mol% (2.6 wt%) UCl_3, while the final composition was 1.13 mol% (6.57 wt%). The OCP values for these two compositions were equilibrium values (e.g., stable over four hours) with the difference in OCP being -22.8 mV. It is very close to the expected OCP difference, -21.4mV calculated from the Nernst equation (Equation 1) at 500°C, assuming the activity coefficient of UCl_3 is constant from 0.43 to 1.13 mol%. The theoretical and measured potential differences were within 7%. The other two OCP values for 0.58 mol% (3.44 wt%) and 0.80 mol% (4.73 wt%) UCl_3 concentrations deviated from the Nernstian expectations. However, for these measurements, approximately only one hour of data was collected following the concentration adjustment so it is likely that equilibrium may not have been reached.

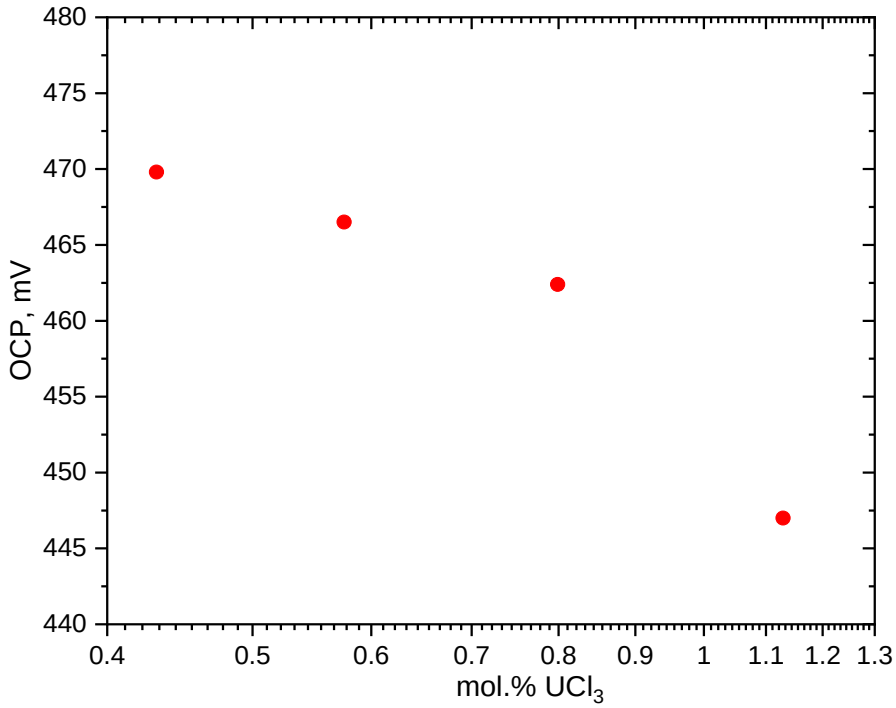

Figure 8. OCP of U-sensor electrode versus Ag/AgCl RE in LiCl-KCl-xUCl_3 salt at 500°C.

Following testing using different UCl_3 concentrations in the salt, further tests were conducted to evaluate sensor sensitivity. Figure 9 shows the measured OCP of the U-sensor after different amounts of $LaCl_3$ and $CeCl_3$ were added into the LiCl-KCl-UCl_3 salt. In this test, the OCP

shifted only slightly and reasonably within the experimental measurement errors. This suggests the U-sensor is insensitive to $LaCl_3$ and $CeCl_3$, while still being sensitive to the UCl_3 concentration shifts. These results are very encouraging and further confirm the effectiveness of the ion exchange process in the formation of the U-β" alumina membrane.

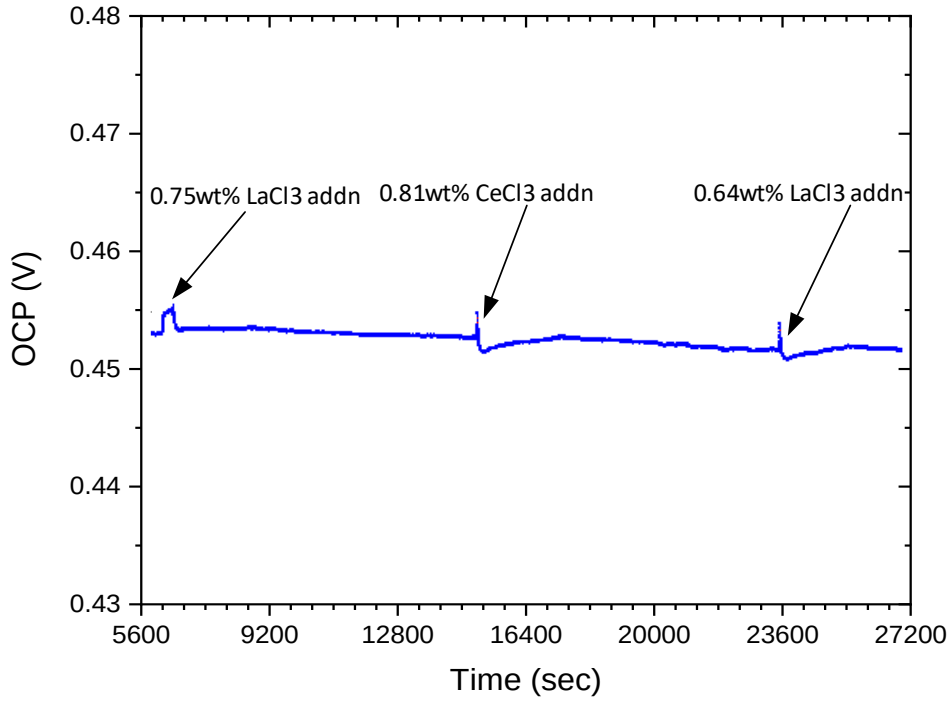

Figure 9. OCP of U-sensor electrode versus Ag/AgCl RE in LiCl-KCl-xUCl_3 when $LaCl_3$ and $CeCl_3$ salts were added.

The sensor was also evaluated in the LiCl-KCl-UCl_3 salt for durations over 500 hours to explore the U-β" alumina membrane compatibility in the salt. Figure 10 shows a photograph of the U-β" alumina membrane in the sensor after > 500 hours of testing. The sensor still had good mechanical integrity with no visible cracks or other defects. This suggests that after all the Na^+ ions in the Na-β" alumina were replaced by the U^{3+} ions from the ion exchange process, the fabricated U-β" alumina tube was compatible with the LiCl-KCl-UCl_3 salt. As a result, the fabricated actinide sensor is expected to operate for a long time without mechanical degradation.

Figure 10. A picture of the U-β” alumina tube after sensor testing, housed in a macor holder.

3.3 Summary

U-β” alumina membranes have been successfully fabricated by ion exchange of Na-β” alumina precursors in UCl_3. U-sensor testing results show that the U-β” membrane can effectively respond to UCl_3 concentration changes, and the selectivity of the U-β” alumina is reasonable. When the system reaches the needed equilibrium, the measured OCP difference due to UCl_3 concentration changes was consistent with that calculated from the Nernst equation. Additional studies are needed to understand the performance of the U-β” alumina membrane as a sensor prior to being applied in the ER.

4 Triple Bubbler

In aqueous reprocessing, a bubbler system is used within the input accountancy tank to determine the total volume (e.g., measures level and assumes density) of acid and dissolved fuel it contains.[18] In an electrochemical facility, the actinide content and salt volume within the batch process vessels (principally the ER) change with every fuel batch, and thus, continuous monitoring is necessary for safeguards. As in the aqueous process, means to monitor the salt volume using a bubbler approach has been explored. Kim et al.[19-20] developed a dynamic bubbler approach in which a single bubbler tube was slowly lowered into a fluid to determine fluid height. Using the dynamic bubbler approach, the salt level was determined within 1.1%.[19] At INL, a triple bubbler approach and instrument have been developed.[21-23] In aqueous testing of the triple bubbler, the density, depth, and surface tension of the fluids were determined to within 0.04%, 0.15%, and 1.25%, respectively.[21] In molten salts testing in the laboratory, the density, depth, and surface tension of molten salts (e.g., LiCl-KCl and cesium chloride [CsCl]-LiCl eutectics) were 0.03%, 0.15%, and 4.6%, respectively.[23] Whereas these studies showed the high accuracy of the triple bubbler approach, they were conducted under ideal conditions in the laboratory over relatively short durations. The goal of the current testing was to explore the triple bubbler performance in an actual electrorefiner under realistic conditions. The approach was to install the triple bubbler into an ER at INL and perform field-testing over extended periods of time. Through these tests, instrument accuracy and uncertainty were evaluated, as well as long-term reliability.

4.1 Experimental Setup

The triple bubbler probe used in these experiments has been described in detail elsewhere.[21-23] To summarize, the triple bubbler consists of three Kovar metal dip-tubes immersed in fluid. A 3D rendering of the triple bubbler is shown in Figure 11. The tube tip inside the radii were 2.28, 1.27, and 2.29 mm for tubes 1, 2, and 3, respectively. A fourth tube was positioned within the bubbler shroud above the salt and was used as a common reference for the differential pressure transducers (DPT) connected to the three dip-tubes. The three DPT were Yokogawa EJA110E calibrated between 0 and 5000 Pa. The three mass flow controllers (MFC) for the individual dip-tubes were MKS type GM50A with a flow configuration between 0 and 6 sccm. Typical flow rates during these experiments were between 2 and 4 sccm.

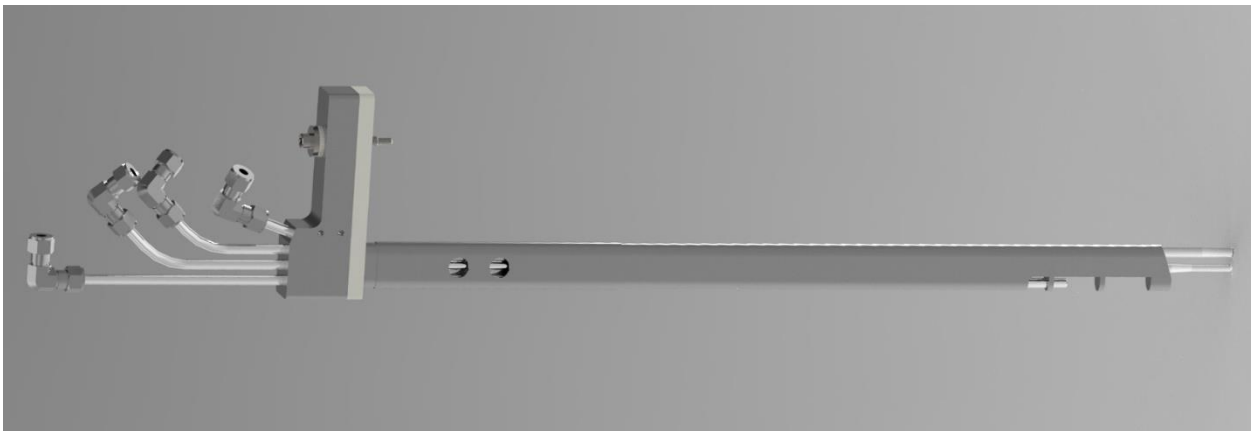

Figure 3. 3D view of the triple bubbler.

Salt within the ER was principally LiCl-KCl eutectic with up to 10 wt% UCl_3 and was operated at 500°C. As the ER had been used in the past to process nuclear fuel, fission product, and rare earth chlorides, as well as other actinides were present in the salt. As a result, the density and surface tension of the salt were unknown and methods to measure them in the hotcell were not available. The salt depth was intended to be measured using a height gauge and contact sensor. However, these measurements proved to be impractical in the ER. As a result, depth measurements in the salt could only be made using a dipstick method. In this approach, a cold SS rod was lowered to the bottom of the vessel and then quickly withdrawn. Salt frozen to the rod (e.g., salt depth) was then measured using calipers. Typically, three to five replicate measurements were taken. As the bubbler was suspended from the top of the ER vessel, the total salt depth (as calculated using bubbler data) is a function of the submerged depth plus the offset between the bottom of the vessel and the bottom of the submerged tubes. The tube offset from the bottom of the vessel was measured (using the height gauge) and had an uncertainty of ± 0.96 mm. The offset was subtracted from the dipstick measurement to arrive at a value that could be compared to the dip-tube submersion depth.

4.2 Results and Discussion

During field-testing, three measurement campaigns were conducted in which the triple bubbler was installed in the ER for extended periods. In the first test, the bubbler operated for

approximately three months, while in the second and third tests, the bubbler operated for about one month each. Figure 12 shows the density and depth measurements over the one-month operation period from the third measurement campaign. In this example, the salt density fluctuated around 1800 kg/m^3 for most of the field-test, while the dip-tube submersion depth varied several cm in depth due to testing designed to simulate tool/electrode insertion and removal.

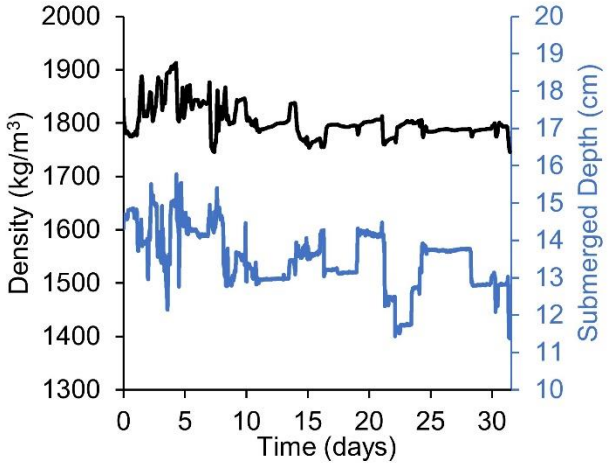

Figure 4. Process monitoring data acquired from the triple bubbler over a thirty-day period. The reported depth is the submersion depth of the bubbler dip-tubes.

Key objectives for the field tests were to determine the measurement uncertainties under realistic conditions and to access the long-term performance of the triple bubbler instrument. In the first measurement campaign, systems were not in place to assess the overall uncertainty and testing was mostly focused on long-term operation and drifts. During the second measurement campaign, all aspects of the triple bubbler system and supporting measurements were evaluated to determine the systematic and random uncertainties in the measurements. The systematic errors came from the following sources: the DPT accuracy, DPT calibration and zero, line losses due to gas flow, and bubbler physical dimensions (e.g., tube radii and lengths). Random uncertainty was determined statistically based on data collected during the field test. Random uncertainty from bubble to bubble was reduced significantly by averaging over several hundred bubble peak pressures (i.e., 3–5 minutes of data). However, there were other random fluctuations that occurred on a larger scale that were not traced to any specific event and could not be easily reduced using averaging. Once the systematic and random contributions to each variable were determined, the relative contributions of each variable to the total uncertainty were evaluated using propagation of error techniques. The largest sources of uncertainty came from the measured pressures followed by the differential tube offset lengths. Overall, the contribution from systematic uncertainties was between 40 and 50%.

Several sets of independent depth measurements were made as a comparison for the triple bubbler accuracy throughout the measurement campaigns. These independent depth measurements were compared to the calculated depths at the time of the measurement, as shown in Table 1. The depth measurements were consistent with the calculated depths from the triple

bubbler. The errors associated with the dipstick approach are high due to difficulties lining up the calipers with the rod in the hotcell, as well as potential bias due to a meniscus on the rod during the dipstick process. The triple bubbler uncertainties reported in the table were determined using a propagation of errors as a function of the random and systematic errors as described above. On average, the overall uncertainty of the triple bubbler submersion depth was 1.12%, which is the best estimate for the depth uncertainty using the triple bubbler under these realistic conditions.

Table 1. Comparison between the calculated dip-tube immersion depth from bubbler data to independent dipstick (minus tube offset) measurements in the ER during three field tests.

	Triple Bubbler (mm)		**Dipstick (minus offset)**		
Field Test #	**Value**	**Uncertainty**	**Value**	**Uncertainty**	**% Difference**
1	131.00	1.50	129	3.5	-1.5
2	143.22	1.57	143.18	3.22	-0.03
2	133.22	1.52	131.83	3.31	-1.05
3	136.29	1.49	134.57	3.37	-1.27
3	129.96	1.45	131.43	3.36	1.12

As mentioned previously, the density and surface tension of the ER salt was not measured directly. Consequently, no comparisons with independent values to assess the accuracy was available. However, uncertainties based on the propagation of errors were determined. For density, the uncertainty was determined to be 0.54% of the measured value. This corresponds to approximately ±10 kg/m^3. The uncertainty for the surface tension was determined to be 12.4%, or approximately ±22 mN/m. The uncertainty on the density is sufficiently low to be useful for material accountancy measurements. The uncertainty on the surface tension is relatively high; however, surface tension is not necessary for determining salt volume, which is determined from depth and density. Therefore, the uncertainty was sufficient for the current application.

During the second field test, an experiment was performed in which salt was removed from the ER to change the salt depth without changing the salt composition. This experiment simulated the removal or insertion of salt, tools, or electrodes that may occur during normal operation of an ER. Two dippers of salt were removed, each consisted of approximately 410 g. While removing the ER baffle to insert the dipper the first time, pressures on P_2 shifted upwards approximately 75 Pa for no apparent reason (e.g., unexplained random fluctuation). However, the shift randomly corrected following the removal of the first dipper and just prior to putting in the second dipper. The depth as calculated from the triple bubbler is shown in Figure 13a using the corrected values for P_2. With the insertion of the dipper, the level increased proportionately to the submerged dipper volume. As the dipper was relatively cold going into the salt, the salt temperatures decreased approximately 30–40°C. When the dippers were removed, the salt level decreased both from the removal of the dipper volume, as well as salt removal. After the second dipper was removed, a depth measurement was taken using the dipstick approach (e.g., 131.83 ± 3.31). Finally, the salt ingots that had been removed by the dippers were added back into the ER one at a time. As the salt temperature varied during this experiment, the density and surface tension also varied a small amount, which explains the gradual rise in salt level following the

return of salt into the ER. This experiment successfully demonstrated that the bubbler could detect abrupt level changes, as well as minor differences due to temperature changes in the salt.

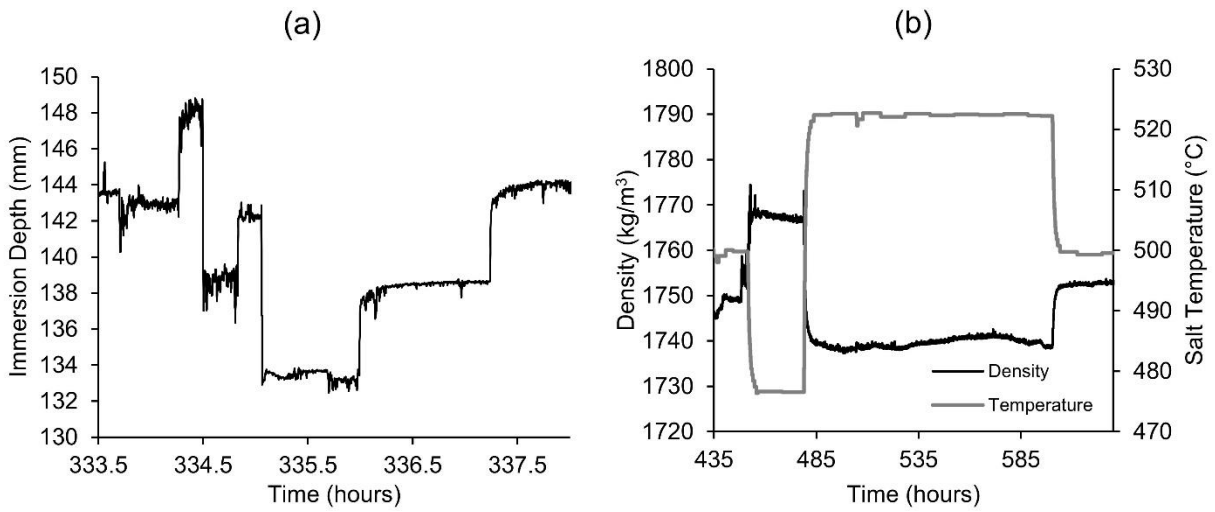

Figure 13. (a) Calculated depth profile during the depth variation test; and (b) plots showing the density and salt temperature throughout the density variation test.

Following depth variation testing, salt temperatures in the ER were manipulated ±25°C to verify the triple bubbler could detect deliberate changes in the density and surface tension due to temperature variation. It is assumed that the above test was applicable to density variations caused by chemical additions as well. In the first step of the experiment, the temperature was lowered to 475°C and left at that temperature for 24 hours. In the next phase, the temperature was raised to 525°C and left for several days. The density throughout the experiment was calculated and is shown in Figure 13b along with the temperature profile over the period. The bubbler was able to detect changes in density as the temperature of the salt was manipulated.

The above independent depth measurements, uncertainty analysis, and variation of ER conditions demonstrated that the triple bubbler could provide accurate and timely process monitoring and nuclear material accountancy measurements. Another main objective in field-testing was to evaluate the long-term operation and reliability of the triple bubbler under realistic conditions. The first time the triple bubbler was installed, it operated for three months before the bubbler tubes became obstructed and completely plugged near where the tubes would have been at the salt freezing temperature (e.g., several cm above the salt line). Dip-tube obstructions were removed using water in the decontamination cell. Since this initial cleaning, the triple bubbler has operated in the ER two additional times, in both cases, after approximately one month of operation, signs of tube plugging reappeared. The water wash approach appears to be an effective maintenance approach to clean the tubes, but is not ideal long-term due to potential corrosion issues. Methods to reduce the plugging effect are being investigated to increase the operation period between maintenance cycles.

4.3 Summary

The triple bubbler instrument has been successfully field-tested in an ER under realistic operating conditions for several months and through three measurement campaigns. The uncertainty of the triple bubbler was determined using a standard propagation of errors approach, which included both systematic and random uncertainties. The uncertainties were ±1.12%, ±0.54%, and ±12.4% for the immersed dip tube depth, salt density, and salt surface tension, respectively. These uncertainties are sufficiently low to allow for the ER vessel salt volume calculations needed to determine the total actinide composition in the ER. Through long-term testing, it was found that the bubbler dip-tubes are prone to plugging and means to reduce the number of maintenance cycles are being investigated.

5 Pu Concentration in U/TRU products using Thermocouple Measurements

During operation of the ER, Pu and other actinides accumulate in the molten salt electrolyte. Periodically, the Pu and U in the salt can be co-extracted in a U/TRU extraction process using a liquid cadmium cathode.[24] The U/TRU product from this operation is predominantly an alloy consisting of U and Pu. Consequently, the means to measure the Pu and U content in the U/TRU product is critical for nuclear material accountancy. A process developed at INL to measure the Pu content of the U/TRU alloy utilizes the unique thermophysical properties (i.e., the solidification curve) of the U/TRU alloys, by monitoring the cooling curves using thermocouples during the solidification process of U/TRU ingots. An inflection in the time versus temperature solidification curves is caused by the latent energy evolved from the alloy on freezing relative to normal heat transport conditions. The temperature at the inflection point can then be translated to liquidus data from established U-Pu phase diagrams for the determination of Pu content. In this work, experiments were conducted in a hotcell to measure U-Pu alloys to evaluate this measurement approach. Two different thermocouple placements (internal and external) were evaluated.

5.1 Experimental Setup and Method

Figure 14a shows a photograph of the furnace (Kerr Corp., Electro-Melt, Model 35224), which featured a two-layer insulation top piece that accommodated thermocouple placement, fixtures for two thermocouples, two thermocouples (Type K), a furnace controller, and a computer for recording temperature and time data. As shown in Figures 14b and 14c, internal to the furnace was a graphite crucible and a grooved alumina block for the placement of the external thermocouple and yttria crucible (Hadron Technologies, Inc., 20 ml). Yttria crucibles were chosen based on their compatibility with molten U and Pu. The alumina block was loaded first into the graphite internal crucible, then the external thermocouple was placed on the alumina block, followed by the yttria crucible. After loading the metal alloy of interest into the yttria crucible, a closed-end alumina tube was placed inside the crucible. The internal thermocouple was then slid down the closed-end alumina tube. Both the internal and external thermocouples sat in grooves in the insulation and were fixed in position by a clamping assembly.

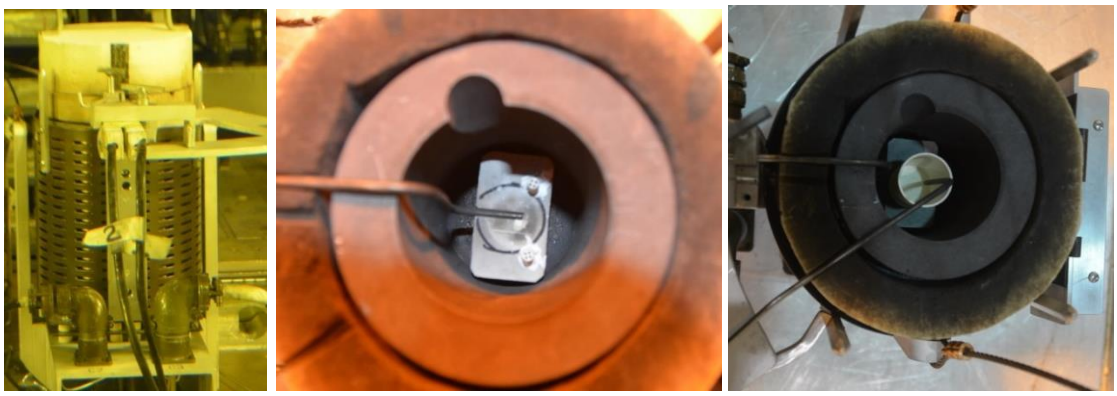

Figure 14. Pictures showing: (a) the furnace inside a hot cell in argon atmosphere; (b) the location of external thermocouple in grooved alumina block; and (c) the internal thermocouple inside of a yttria crucible.

Metals and alloys investigated in the hotcell were Ag, aluminum (Al), and U-Pu alloys. The Al (Thermo Fisher, 4-8 mm shot, 99.999%) and Ag (Alfa Aesar, 1 mm, 99.9%) were chosen for testing and furnace characterization. Amounts of these initial test materials were selected to approximate and/or bracket a 50% U – 50% Pu alloy (e.g., the representative alloy based on the MPACT Virtual Facility Distributed Test Bed of an electrochemical reprocessing facility).[1] The thermophysical properties of interest in this study are the melting temperature, heat of fusion, and heat capacity, all of which are shown in Table 2 for the different metals.[25-27] The heat of fusion is a measure of the heat evolved per gram during solidification while the heat capacity is the heat given off with temperature change. The heat of fusion for the 50% U-50% Pu alloy was estimated using weighted averages of the heat of fusions for pure metals. Also shown in the table is the heat energy loss required to solidify the entire sample.

Table 2. Thermal properties for 50% Pu-50% U alloy, aluminum, and silver for given masses.

Metal	Mass (g)	Melting Temperature (°C)	Heat of Fusion (J/g)	Heat Capacity (J/K)	Heat Energy (J)
50% U-50% Pu	100	825	23.57	19	2357
Al	12	660	410.25	15	4923
Ag	29	962	104.41	9	3028

5.2 Results and Discussion

The first experiments performed in the hotcell were done using surrogate materials. Figure 15a and 15b shows the furnace characterization data for the internal and external thermocouples with 29 g of pure Ag metal and 12 g of pure Al, respectively. These figures are plots typical of temperature profiles generated during the furnace characterization. During cooldown, the external thermocouples temperatures were slightly higher than the internal thermocouple temperatures as was expected due to heat transfer from the furnace through the crucible and finally into the molten metal. From the temperature profile itself, it was difficult to pinpoint the exact temperature of solidification. However, when the first derivates of the temperature profiles are plotted, as shown on the secondary (right-hand) y-axis, the temperature inflection point

becomes more pronounced. For both Ag and Al, the internal and external thermocouples provided simultaneous responses to indicate time and temperature of solidification. This suggests that the external thermocouple could be used by itself to monitor the solidification temperature if necessary.

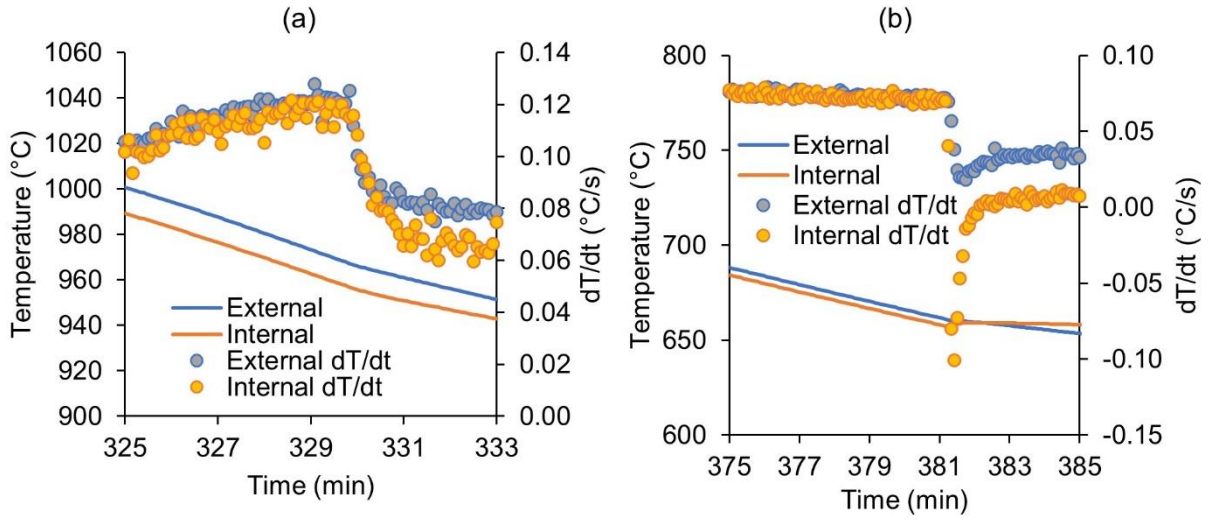

Figure 15. External and internal thermocouple temperature and derivative data for: (a) Ag; and (b) Al.

The temperature difference (or bias) between thermocouple measurements and the actual melting temperature of metal needed to be established to "calibrate" the furnace setup. The measured melting points for pure Ag and Al using internal thermocouples were compared against the actual melting points of the same metals. The differences between the measured and known melting temperatures were -0.52% and -0.17% for Al and Ag, respectively. Differences in the measurements were within the uncertainty ($\pm$ 0.75%) for Type K thermocouples giving confidence in the internal measurements. The average difference between the external and internal thermocouples at the inflection points was 12.45 °C and 4.55 °C for Ag and Al, respectively.

Following characterization of the thermocouples with pure Al and Ag, three U/TRU alloys were studied, and the mass and compositions of the alloys are shown in Table 3. The Pu and U contents were measured using analytical chemistry and the other constituents (actinides and a couple hundred ppm rare earths) were calculated by mass balance. The first U/TRU material (alloy #1) was tested using both the internal and external thermocouples. In the second and third tests, only the external thermocouples were used.

Table 3. Masses and composition of U/TRU alloys utilized for solidification testing.

U/TRU Alloy	Thermocouples	Mass (g)	Total Pu (wt%)	Total U (wt%)	Other (wt%)
1	Internal & External	66	47.5	52.22	0.28
2	External	81	37.86	61.92	0.22
3	External	97	32.12	67.71	0.17

Shown in Figure 16a are the temperature versus time data from the internal and external thermocouples for the two heat ups performed on the U/TRU alloy #1. In this test, the alloy was put through two heating and cooling cycles. Figure 16b shows a detailed view of the second cooldown cycle of alloy #1 and includes the derivative of the temperature/time data on the right-hand y-axis. From the derivative data on both the internal and external thermocouples, the liquidus transition is obvious and occurs at approximately 389 minutes. The internal and external temperature measurements at the liquidus transition point, as well as the difference between the thermocouples, are given in Table 4.

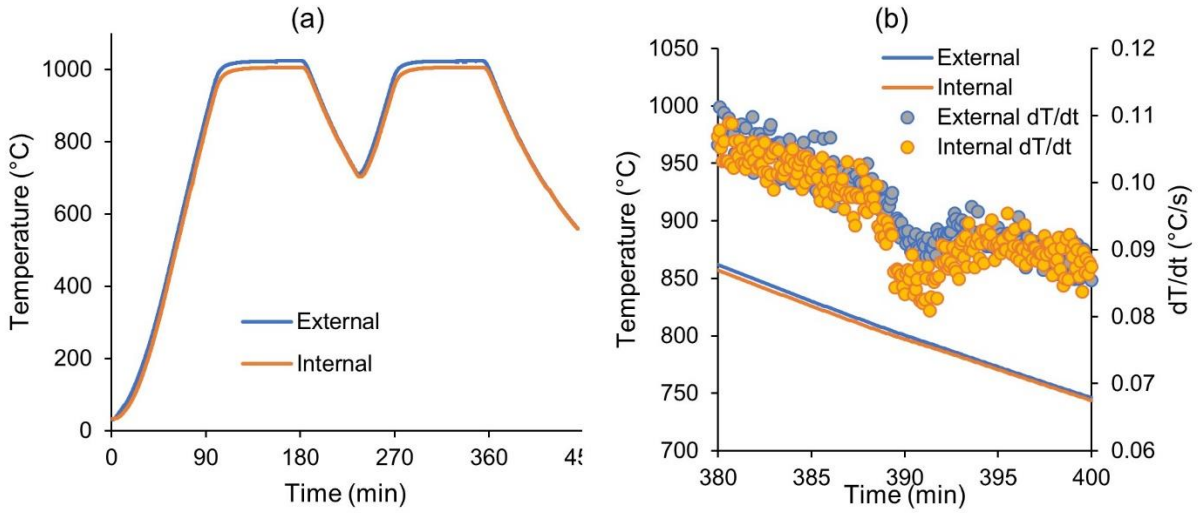

Figure 16. Results from U/TRU alloy #1: (a) temperature versus time data from the internal and external thermocouples; and (b) derivative analyses of the second cooldown period.

Table 4. Comparison of internal and external thermocouple data for U/TRU alloy #1 cooldowns.

Cooldown	Internal (°C)	External (°C)	Difference (°C)
1	806.32	810.66	4.34
2	800.07	803.8	3.73

The difference between the internal and external thermocouples for alloy # 1 was on average 4 °C. The temperature difference between the thermocouples just as the melt approaches the solidification temperature is correlated to the heat capacity of the material. The largest temperature difference occurred for Ag with the lowest heat capacity while the smallest temperature difference occurred for the U-Pu alloy, where the heat capacity was larger. No heat transfer modelling was done to predict the difference between the internal and external thermocouples for the Al, Ag, and U-Pu alloys. However, as the heat capacity of U and Pu are relatively similar, the value was not expected to shift dramatically with the U-Pu alloy composition. As a result, the average differential of 4 °C observed in the alloy #1 test was adapted as a correction for the other two alloys measured in the same furnace/insulation setup. Table 5 shows external temperatures where an indication of the liquidus transition occurs according to derivative data and calculated internal temperatures for U/TRU alloys #2 and #3.

Table 5. External and calculated internal temperatures for U-TRU alloys #2 and #3.

U/TRU Alloy	Cooldown	External (°C)	Estimated Internal (°C)
2	1	897.2	893.2
2	2	887.46	883.46
3	1	925.51	921.51
3	2	926.53	922.53

Figure 17 shows liquidus temperature data as a function of Pu content (e.g., phase diagram) from several investigators.[25, 27-31] The relationship between the alloy melting/freezing temperature between 0.3 mol% and 1 mol% U formed a linear relationship with an R^2 value of 0.9949. From the linear regression equation, the measured solidification temperatures could be directly correlated to the Pu concentration. The Pu content was calculated for the three alloys. Results are shown in Table 6. Also included in the table are the Pu contents measured from analytical chemistry samples. By comparing the calculated Pu content from the cooling curve measurement and from the analytical chemistry, the percent error was calculated and is shown in the table as well. The percent difference for the first measurement on U/TRU alloy was 9.27%, which is high uncertainty for materials accountancy purposes. Two possible explanations for the large percent difference in the U/TRU alloy #1 Pu contents may be the smaller mass (66 g) or the fact that this material went through multiple heating/cooling cycles prior to this analysis. After the masses of the U/TRU alloys were increased to 81 g (for alloy #2) and 97 g (for alloy #3), the percent difference was improved significantly, at 4.19% and 5.15%, respectively. The uncertainty for the measurements as determined using propagation of errors was on average 5% for the different alloys investigated. Consequently, the uncertainty with this approach is estimated to be within ± 5%. The Pu contents as measured using analytical chemistry versus the calculated liquidus temperatures are plotted in Figure 17. This provides a visual representation of the accuracy of the thermocouple measurements and shows that the measured liquidus results are consistent with other works from literature.

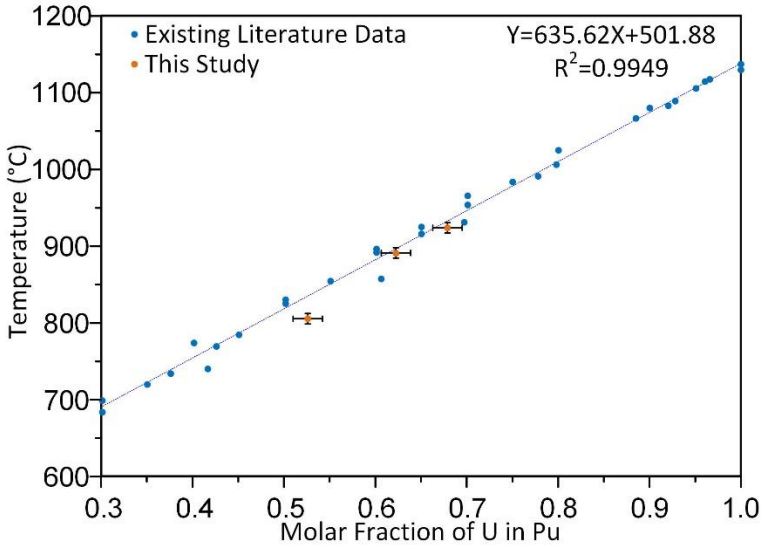

Figure 17. Portion of the U-Pu phase diagram drawn from multiple literature sources[25, 27-31] with regressed equation and data from this study.

Table 6. Measured and calculated Pu contents for the three U/TRU alloys tested.

U/TRU Alloy	Mass (g)	Measured Total Pu (wt%)	Calculated Total Pu (wt%)	% Error
1	66	47.5	52.12	9.27
2	81	37.86	39.48	4.19
3	97	32.12	33.82	5.15

In the three experiments conducted using U/TRU alloys, the calculated Pu content was always higher than measured using analytical chemistry measurements. The most probable explanation was oxidation of the alloys during sampling in the hotcell or prior to analyses in the analytical laboratory. If oxidation occurred, it would result in slightly lower Pu content measurements. For example, the U/TRU alloy #3 ingot was analyzed using non-destructive assay (NDA) techniques (fast neutron energy multiplication and precision gamma scanning) prior to sampling for destructive analytical chemistry analysis. Differences between the NDA and sample analytical results showed the same bias with the Pu content from NDA being slightly higher than the analytical chemistry results. Another explanation, or contributing factor, to the higher observed Pu content from the thermocouple measurements may be due to minor temperature differentials across either the alumina sheathing (internal) or yttria crucible (external) that was not directly addressed in this study. In other words, the actual temperature of the alloy on solidification may be slightly higher than were measured at the thermocouples since the sheathing and crucible provided some degree of insulation. The measurement accuracy is expected to be improved after addressing the potential oxidation issues in sampling, and more particularly, the temperature differential across the thermocouple sheathing and crucible.

5.3 Summary

An in-situ actinide monitor has been developed and demonstrated to measure Pu content during a casting type operation using both internal and external thermocouples. There appears to be a slight bias in the calculated to measured % Pu to overpredict the Pu content. Despite the observed bias, the error was typically within ±5% for the measurement approach.

6 Conclusions

As part of the Virtual Facility Distributed Test Bed of an electrochemical reprocessing facility being developed under the U.S. DOE MPACT program, INL has developed four technologies that can be integrated into the facility design to provide greater confidence in process monitoring and nuclear material accounting and control. These technologies are: OR voltammetry, ER actinide sensor, ER triple bubbler, and U/TRU analysis via thermocouple measurements.

The OR voltammetry probe was designed to be integrated into an OR furnace to monitor for undeclared or abnormal activity in which actinide chlorides become present. The probe consists of two Ni/NiO RE, a SS CE, and an Ir WE, as well as a SS WE. The probe was installed into an OR at INL and successfully completed over nine months of weekly testing in the salt. During these tests, there was no observed degradation of the CV measurements over time. In addition, the CV measurement scans were consistent over periods of inactivity in the OR and provided useful process monitoring data during OR operations. The CV scans were able to identify the presence of LiCl, Li_2O, and LiOH; no other chlorides were detected in the scans.

The ER actinide sensor consisted of an Ag/AgCl RE and U- β" alumina membrane electrode. The U-membrane was manufactured from a Na-β" alumina that was ion-exchanged at 735°C in solid UCl_3. This new U-β" alumina material appeared to have good mechanical properties and did not crack or spall throughout the manufacturing or testing process. The sensor was tested in LiCl-KCl salt with four different concentrations of UCl_3. As the UCl_3 concentration shifted, the measured OCP shifted as expected. Under equilibrium conditions, the measured difference in OCP was within 7% of the theoretical difference in the OCP based on the Nernst equation. In addition, an experiment was performed in which $LaCl_3$ and $CeCl_3$ were added to the salt to test the sensor sensitivity to elements outside of UCl_3. The results showed very little change in the OCP measurements with the addition of these rare-earth chlorides. Finally, after over 500 hours of operation, the sensor appeared to be in good mechanical health.

The triple bubbler probe was designed to monitor the salt level and density in the ER. With these measurements, the total mass of U and Pu could be determined in combination with analytical data. The triple bubbler consisted of three bubbler dip-tubes immersed in the salt. The bubbler completed three successful measurement campaigns in an ER at INL. During these tests, the bubbler tube depth was determined and compared to independent dipstick measurements, and in all cases, the two depth values agreed within uncertainty. The overall uncertainties of the bubbler measurements were also determined to be 1.12%, 0.54%, and 12.4% for depth, density, and surface tension, respectively. Through testing, it was found that the bubbler dip-tubes were susceptible to plugging and a cleaning process was necessary every 1000–3000 hours of operation.

A method to measure the Pu concentration of U/TRU alloys from a U/TRU extraction process using thermocouple measurements of the alloy during cooling has been developed and tested. The approach was to melt the alloy and then allow it to cool while monitoring the temperature using internal and external thermocouples. Once the solidification temperature was determined, U-Pu phase diagrams were used to determine the Pu concentration. Three U-Pu alloys were tested in the hotcell at INL. The first alloy incorporated both the internal and external thermocouples and a relationship between the two thermocouples was determined. The other two alloys were tested using only external thermocouples. The % errors between the Pu concentration as measured using analytical chemistry and the U/TRU measurement method were 9.73%, 2.5%, and 5.07% for alloys #1, #2, and #3, respectively. The larger error of the first sample was contributed to the smaller mass size (66 g) of the sample and because more heating and cooling cycles were performed on the material, alloying for a greater degree of oxidation. Overall, it is estimated that the uncertainty of this approach is ±5%.

7 Acknowledgements

This work was supported by the U.S. Department of Energy, Office of Nuclear Energy, under DOE Idaho Operations Office contract DE-AC07-05ID14517. Accordingly, the U.S. Government retains and the publisher, by accepting the article for publication, acknowledges that the U.S. Government retains a nonexclusive, paid-up, irrevocable, worldwide license to publish or reproduce the published form of this manuscript or allow others to do so, for U.S. Government purposes. The authors want to thank Drs. Steven Herrmann, Rob Hoover, Ken Marsden, and Prabhat Tripathy for their assistance and support. Finally, we wish to thank Mr. Dean Burt and Mr. Ronald Wallace for laboratory support and fabrication services.

Authors Brian Westphal, Shelly Li, Brenda Serrano-Rodriguez, and Natalie Gese are former INL employees who had contributed to these projects while at INL. For their current affiliations, please contact the corresponding author.

8 References

1. Cipiti, B.B., Browne, M., and Reim, M. 2021. The MPACT 2020 Milestone: Safeguards and Security by Design of Future Nuclear Fuel Cycle Facilities, *J. Nucl. Mater. Manage*, Vol. X, No. X.

2. Hoyt, N.C., Launiere, C.A., and Stricker, E.A. 2021. In-Process Monitoring of Molten Salt Composition by Voltammetry and Automated Sampling-based Techniques, *J. Nucl. Mater. Manage*, Vol. X, No. X.

3. Nagai, T. et al. 2005. Redox Equilibrium of U 4+/U 3+ in Molten NaCl-2CsCl by UV-Vis Spectrophotometry and Cyclic Voltammetry, *J. Nucl. Sci. Technol.* 42: 1025–1031.

4. Lim, K.H. and Yun, J.I. 2019. Study on the exchange current density of lanthanide chlorides in LiCl-KCl molten salt, *Electrochim. Acta*, 295: 577–583.

5. Yoon, D. and Phongikaroon, S. 2015. Electrochemical Properties and Analyses of CeCl 3 in LiCl-KCl Eutectic Salt, *J. Electrochem. Soc.*, 162: E237–E243.

6. Yoon, D. et al. 2019. Determination of kinetic properties of Sm(III)/Sm(II) reaction in LiCl–KCl molten salt using cyclic voltammetry and electrochemical impedance spectroscopy, *J. Radioanal. Nucl. Chem.* 322: 1031–1037.

7. Williams, A.N., Cao, G., and Shaltry, M.R. 2020. Voltammetry measurements in LiCl–Li_2O salts: An evaluation of working electrode materials, submitted to *J. Nucl. Mater.*

8. Gonzalez, M. et al. 2018. Identification, measurement, and mitigation of key impurities in LiCl-Li2O used for direct electrolytic reduction of UO_2, *J. Nucl. Mater.* 510: 513–523.

9. Gese, N.J. and Pesic, B. 2013. Electrochemistry of LiCl-Li2O-H2O Molten Salt Systems, in: 2013 TMS Annu. Meet. Exhib. San Antonio, TX.

10. Dunn, B. and Farrington, G.C. 1983. Trivalent ion exchange in beta″ alumina, *Solid State Ionics.* 9–10: 223–225.

11. Schäfer, G.W. and Weppner, W. 1992. Preparation of divalent beta-alumina ceramics via ion exchange from K- and Na-β″-alumina ceramics, *Solid State Ionics.* 53–56: 559–563.

12. Sattar, S. 1986. Synthesis of di- and trivalent by ion exchange, *J. Solid State Chem.* 1986: 231–240.

13. Koh, J.H., Weber, N., and Virkar, A.V. 2012. Synthesis of lithium-beta-alumina by various ion-exchange and conversion processes, *Solid State Ionics*. 220: 32–38.

14. Ghadbeigi, L. et al. 2016. Synthesis of iron-doped Na-β"-alumina + yttria-stabilized zirconia composite electrolytes by a vapor phase process, *Solid State Ionics*. 290: 77–82.

15. Parthasarathy, P., Weber, N., and Virkar, A.V. 2007. High temperature sodium - zinc chloride batteries with sodium beta - alumina solid electrolyte, *ECS Trans.* 6: 67–76.

16. Virkar, A. 2008. A high temperature electrochemical energy storage system based on sodium beta"-alumina solid electrolyte (BASE), DE-FC26-05NT42623.

17. Ionotec. 2020. Available at http://www.ionotec.com.

18. Janssens-Maenhout, G., Dechamp, L., and Grassi, P. 2004. Monitoring of the interface movement of a bubbling dip tube by the pressure signal, CHISA Conference, Prague, Czech Republic, August 2004.

19. Kim, J.Y. et al. 2017. Automated high-temperature liquid level measurement system using a dynamic tube pressure technique, *J. Indust. Eng. Chem.* 49: 30–35.

20. Kim, J.Y. et al. 2020. Wireless simultaneous measurement system for liquid level and density using dynamic bubbler technique: Application to KNO3 molten salts, *J. Indust. Eng. Chem.* 82: 57–62.

21. Williams, A.N., Galbreth, G.G., and Sanders, J. 2018. Accurate determination of density, surface tension, and vessel depth using a triple bubbler system, *J. Indust. Eng. Chem*. 63: 149–156.

22. Williams, A.N. et al. 2019. Application of a triple bubbler sensor for determining the density, surface tension, and depth in molten salts, *J. Nucl. Mater. Manage*. XLVII: 47–52.

23. Williams, A.N. 2020. Application and testing of a triple bubbler sensor in molten salts, *Nucl. Eng. Technol.* 52: 1452–1461.

24. Vaden, D. et al. 2008. Engineering-scale liquid cadmium cathode experiments, *Nucl. Technol.* 162: 124–128.

25. Janney, D.E. and Papesch, C.A. 2015. FCRD Transmutation Fuels Handbook 2015, INL/EXT-15-36520, Idaho National Laboratory.

26. McDonald, R.A. 1967. Enthalpy, heat capacity, and heat of fusion of aluminum from 366° to 1647°K, *J. Chem. Eng. Data*. 12: 115–118.

27. Arblaster, J.W. 2015. Thermodynamic properties of silver, *J. Phase Equilibria Diffus.* 36: 573–591.

28. Ellinger, F.H., Elliott, R.O., and Cramer, E.M. 1959. The plutonium - uranium system, *J. Nucl. Mater.* 1: 233–243.

29. AEC Research and Development Report. 1967. Mound Laboratory Report MLM-1445.

30. Okamoto, Y. et al. 1994. Investigation of the PuU phase diagram, *J. Alloys Compd.* 213–214: 372–374.

31. Westphal, B.R. and Li, S.X. 2019. Evaluation of experimental studies in the U-rich region of the U-Pu Phase diagram, *Metall. Mater. Trans. B.* 50B: 799–807.